Journal of Volcanology and Geothermal Research 411 (2021) 107124

Contents lists available at ScienceDirect

Journal of Volcanology and Geothermal Research

journal homepage: www.elsevier.com/locate/jvolgeores

Short communication

Sentinel-1 InSAR captures 2019 catastrophic White Island eruption

Mark Harvey

Harvey Geoscience Ltd, 51 Gifford Rd, West Hartford, CT, USA

ARTICLE INFO

Article history:
Received 25 March 2020
Received in revised form 18 November 2020
Accepted 19 November 2020
Available online 02 January 2021

Keywords:
InSAR
StaMPS
PS
Sentinel
White Island
Volcano eruption

ABSTRACT

The andesitic volcanic island Whakaari (White Island) explosively erupted on 9 December 2019. White Island is a popular tourist destination, and 47 people were on the island at the time. Twenty-one died, and a further twenty-six people suffered injuries. Persistent scatterer (PS) interferometry with synthetic aperture radar (SAR) is a powerful satellite-based remote sensing tool to monitor land deformation associated with volcanic unrest. This study examined deformation on White Island over the eruption period and identified a dome on the crater floor that inflated for 15 months preceding the eruption, consistent with a previous analysis of TerraSAR-X satellite data. Results here show the dome began to collapse after 25 November, about two weeks prior to the eruption. This finding has immediate relevance for ongoing hazard monitoring at White Island and other volcanoes worldwide where sudden dome contraction may presage an eruption.

1. Introduction

Whakaari (White Island) is the exposed summit of an active stratovolcano located ~50 km offshore Whakatane, New Zealand (Nairn et al., 1996) (Fig. 1). Frequent episodes of unrest are usually associated with crater floor deformation (Hamling, 2017; Fournier and Chardot, 2012; Peltier et al., 2009), increased seismicity (Sherburn et al., 1998) and gas emissions (Giggenbach, 1987). Recent activity is characterised by high temperature fumarolic emissions (Harvey et al., 2015; Giggenbach, 1987; Clark, 1973), and episodic phreatomagmatic eruptions inferred to originate at shallow depths (<1.0 km) (Walsh et al., 2019; Jolly et al., 2017; Nishi et al., 1996); leveling data recorded since the 1960's indicates crater-floor deformation results from shallow (10's – 100's of meters) hydrothermal activity (Fournier and Chardot, 2012; Peltier et al., 2009; Clark and Otway, 1989), rather than deeper magmatic processes.

Prior to December 2019, the most recent eruption of White Island occurred on 27 April 2016. The eruption was preceded by a period of heightened volcanic tremor and lowering of crater lake water level, but two Global Navigation Satellite System (GNSS) monitoring stations on the island showed no deformation either before or after the eruption (Hamling, 2017).

Interferometric synthetic aperture radar (InSAR) monitoring showed the crater floor was stable from mid-2017 to early-2018, then acceleration of crater floor inflation beginning mid-2018 (see A4 and D4, Fig. 4 in Hamling, 2020; Cao et al., 2020). Real-time seismic amplitude measurements (RSAM) showed an increasing trend from June 2019 (Park et al., 2020). On 18 November 2019 an alert bulletin reported an increase in magmatic degassing (SO_2) and volcanic tremor (weak to moderate strength), but no change in the locations and frequency of earthquakes near the island (Geonet, 2019).

White Island explosively erupted 9 December 2019. 47 people were on the island, of which twenty-one died, and twenty-six suffered injuries. Many injured suffered serious burns after being covered in hot ash. This event illustrates the necessity of efficient and safe monitoring of volcanoes, especially those with a large number of visitors.

In this study Sentinel-1 data is processed using the Stanford Method for Persistent Scatterers (StaMPS) (Hooper et al., 2012), an established method for time series analysis of InSAR data (Osmanoğlu et al., 2016) that was previously used to map deformation in the Taupo Volcanic Zone (TVZ) related to hydrothermal depressurisation (Harvey et al., 2019; Hamling et al., 2016). The StaMPS method identifies persistent scatterers (PS), surface objects that reflect incoming radar signals with stable phase characteristics in space and time (Hooper et al., 2004). PS methods such as StaMPS allow the motion of each PS to be very precisely measured (~ mm/year), and ground deformation to be mapped.

2. Sentinel-1 processing workflow

Processing of Sentinel-1 data was conducted using open source software including the Sentinel Application Platform (SNAP - ESA Sentinel Application Platform v 7.0.0, http://step.esa.int) and StaMPS (Hooper et al., 2012). In StaMPS analysis, interferograms are formed between a single primary image and a number of secondary images acquired on

E-mail address: mark@harveygeoscience.com.

https://doi.org/10.1016/j.jvolgeores.2020.107124
0377-0273/

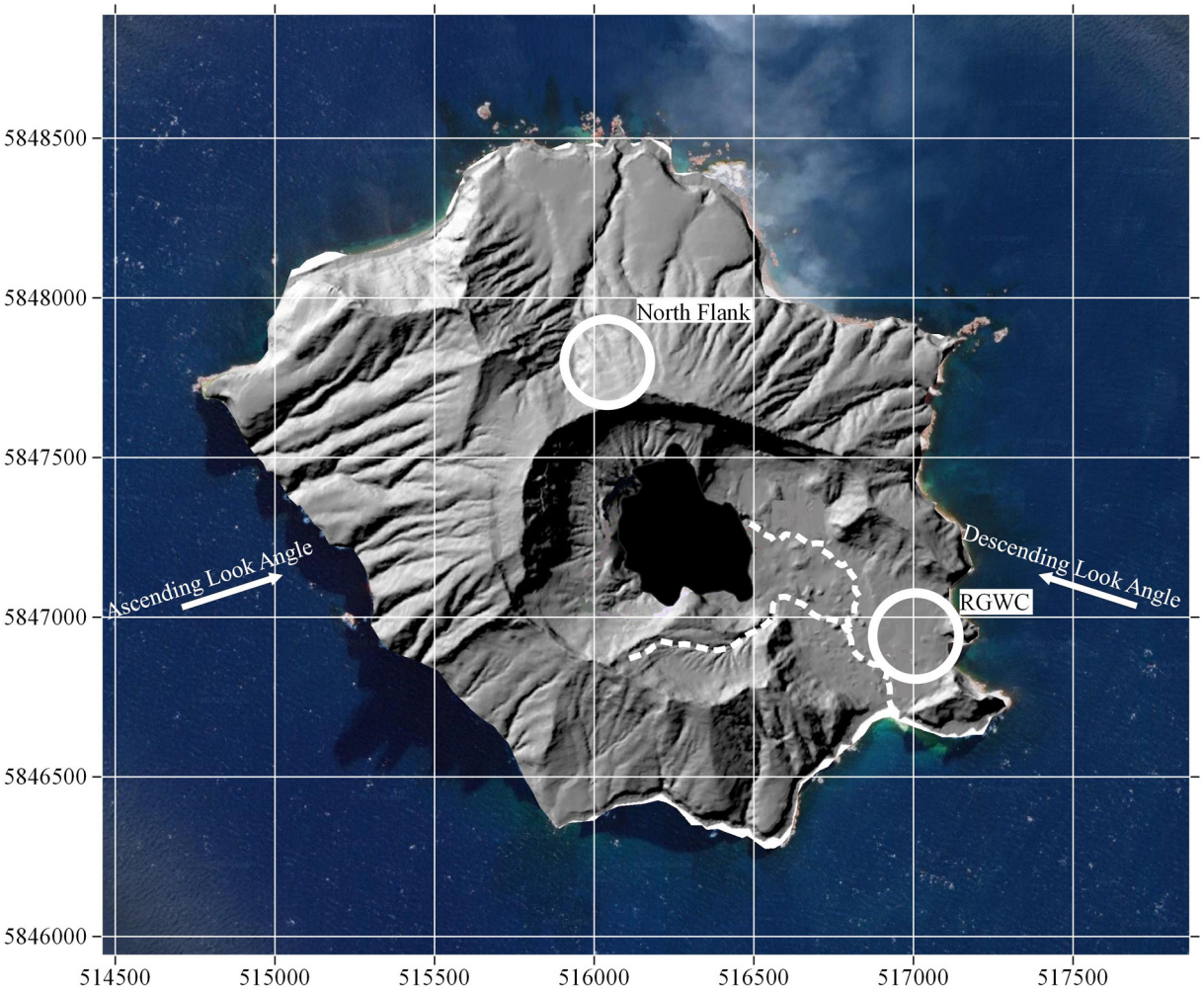

Fig. 1. Digital surface model of White Island, New Zealand (modified after Kilgour et al., 2019). White dash line shows tourist trail from boat landing into crater. White circles show datum areas (StaMPS processing reference areas). Arrows show Sentinel-1 satellite look-angles for ascending and descending tracks. Map grid units are meters (WGS84). Solid black area at centre is the crater lake.

different dates. The first step was to extract the study area from satellite data using SNAP, which reduced the size of data and decreased processing time.

The second step was to compute individual interferograms using SNAP, combining the single primary image with secondary images. The resulting stack of interferograms were input to StaMPS for PS analysis. StaMPS then outputs time series and velocity for all PS in the area of analysis for the time interval of observation. Three tracks were processed, each of which provide separate time series of ground deformation. In addition, each track was processed twice giving longer and shorter stacks (Table 1). The purpose of the longer stacks was to provide a longer record of deformation (back to mid-2018). The purpose of the shorter stacks was to decrease temporal decorrelation (Malinverni et al., 2014), thus increasing spatial density and coverage of PS.

Velocities were reported relative to two reference areas (datums) on White Island. The first datum was based on the average motions of PS within a 100 m radius of the White Island Crater Floor GNSS continuous monitoring station (RGWC) (Fig. 1). RGWC has shown no long-term trend in vertical motion since mid-2018 (Fig. 2A) (Geonet, 2020a). A common datum allows combination of LOS motions from ascending and descending tracks to estimate vertical and eastward velocities (Manzo et al., 2006). The second datum was based on the average motions of PS within a 100 m radius area on the north flank of the volcano (Fig. 1). This provided a frame of reference external to the crater floor, which improved sensitivity to short-term motions on the crater floor. Vertical time series for RGWC showed the short-term signal was unstable (average daily elevation change of 4 mm over the study period) (Appendix A, Fig. S1). Following StaMPS convention, time series units are millimetres, with a positive slope indicating LOS motion towards the satellite.

Atmospheric effects correlated with topography were previously observed on large stratovolcanoes (e.g. Mt Etna and Mt Llaima), visible in interferograms as concentric fringes centred on the volcanic edifice (Parker et al., 2015), however no such fringes are visible in White Island interferograms (interferograms and time series are provided as supplementary data, Appendix A). Stratigraphic atmospheric effects are caused by vertical stratification of atmospheric moisture in areas of significant topographic relief (Parker et al., 2015). However, White Island has very small subaerial relief and area (300 m/4 km^2) compared to Mt Etna (3000 m/1000 km^2) or Mt Llaima (2000 m/300 km^2). Although stratified effects are considered extremely unlikely at White Island, StaMPS processing was undertaken with filtering to address noise coming from possible atmospheric disturbance (Hooper et al., 2012).

Interpolation of PS velocity point data was undertaken by ordinary kriging using SAGA (System for Automated Geoscientific Analyses), which provided LOS deformation maps for ascending and descending tracks. Omnidirectional variograms show smooth upward slopes and were modelled for kriging (variograms are provided in Appendix A,

Table 1
Sentinel-1 satellite data.

Track pass	Stack size	First image	Last image	Track	Sub-Swath	Burst
73	44	2/08/2018	12/01/2020	Descending	IW1	6 to 7
73	20	17/05/2019	12/01/2020	Descending	IW1	6 to 7
175	44	9/08/2018	19/01/2020	Descending	IW3	2 to 3
175	20	24/05/2019	19/01/2020	Descending	IW3	2 to 3
8	44	4/08/2018	14/01/2020	Ascending	IW2	5 to 6
8	20	19/05/2019	14/01/2020	Ascending	IW2	5 to 6

Fig. S2). The smooth slopes confirm spatial autocorrelation (Moran, 1950), and the applicability of kriging to interpolate the normally-distributed datasets.

Ascending and descending deformation maps were combined in QGIS (*Raster Calculator* tool) to provide approximate vertical displacement (d_z) (see Eq. 2 in Manzo et al., 2006):

$$d_z \approx \frac{(d_{LOS\_Desc} + d_{LOS\_Asc}/2}{\cos\theta} \quad (1)$$

similarly, the east-west displacement component (d_{east}) was estimated (see Eq. 1 in Manzo et al., 2006):

$$d_{east} \approx \frac{(d_{LOS\_Desc} - d_{LOS\_Asc}/2}{\sin\theta} \quad (2)$$

Where d_{LOS_Desc} is LOS motion from the descending pass, d_{LOS_Asc} is LOS motion from the ascending pass, and θ is the average elevation angle (radians) for descending and ascending passes. The above equations assume: i) no north-south motion, ii) the same elevation angles at White Island for ascending and descending satellite passes (actual angles are 33.4° and 36.7° for track #8 and #175 respectively), and iii) the LOS velocity is constant in time. Error relating to the final assumption is minimised by restricting calculation of vertical and eastward motion to separate periods; a pre-eruption period (green area Fig. 2) and an eruption period (orange area Fig. 2), where time series are approximately linear (i.e. velocity is constant).

3. Deformation on White Island

RGWC-datum PS maps for the 15-month pre-eruption period (August 2018 – November 2019, green area of time series in Fig. 2) show zones of contrasting LOS motion (east-lake and west-lake zones, Fig. 2). Ascending and descending tracks were combined to solve for vertical and horizontal motion and confirm the zones (Fig. 3A & C). The vertical deformation map (Fig. 3A) was used to create the zone boundaries. Time series (Figs. 2 and 5) are based on the average of PS selected from the east-lake zone. Similar opposing zones were previously observed at White Island following the 2016 eruption (see Fig. 4 in Hamling, 2017). The vertical deformation map shows the east-lake zone is an inflating dome (Fig. 3A), consistent with the 'inflation source' from Hamling (2017) (white parallelogram in Fig. 2 of that study). Hamling (2017) attributed the inflation to pressurisation of the shallow hydrothermal system. The west-lake zone subsides (Fig. 3A) and moves eastward (Fig. 3C), as previously observed in the southwest crater following the 2016 eruption and loss of lake water (Hamling, 2017). Motion in east-lake and west-lake zones agrees with a more recent TerraSAR-X based study that reported east-lake inflation, and west-lake slope collapse during 2019 (Hamling, 2020, see Fig. 4 in that study). The subsidence of the west-lake zone may have been captured by the nearby RGWI GNSS station, which showed downward motion from mid-2019 (Fig. 2C) (Geonet, 2020b).

Vertical (Fig. 3B) and horizontal (Fig. 3D) motions were estimated for the eruption period (November 2019 – January 2020, orange area of time series in Fig. 2), which shows reversal of motion for east-lake and west-lake zones; vertical deformation shows the dome collapses and the previously subsiding west-lake zone changes to uplift (Fig. 3B). The dome collapse suggests depressurisation of the shallow hydrothermal system occurred during the eruption period.

A similar reversal of horizontal motions is observed; the 'inflation source' area reverses to eastward motion, while the west-lake zone moves westward (Fig. 3D). The reversal may be caused by intrusion of magma beneath the crater lake area, displacing surrounding volumes and surfaces upward and outward, away from the central conduit. This could also explain the obvious uplift of the west-lake area (Fig. 3B), and more widespread (but subtle) inner-crater uplift zone that surrounds the deflating dome (Appendix A, Fig. S4). A magmatic intrusion is supported by the appearance of lava (January 2020) in crater vents created by the eruption (Geonet, 2020c).

Eruption period deformation maps (Fig. 3B and D) are based on linear regression of a shorter (2.5 month) section of the time series, with greater standard deviations (orange area of time series in Fig. 2). Accordingly, velocities in the eruption period deformation maps are more approximate than for the pre-eruption deformation maps (Fig. 3A and C). However, maps derived from tracks #8 and #73 are nearly identical, showing both vertical and horizontal reversals (Appendix A, Fig. S3), which supports the observation of reversal described above.

Cumulative displacement for the dome was determined by integrating vertical velocity over the 15-month pre-eruption period (Appendix A, Fig. S5), then used to invert for depth and volume of the inflation source (Mogi, 1958). A Monte-Carlo simulation (1000 realisations) minimised square misfit between observed and calculated displacements (Fig. 4). This gave estimates of depth (~100 m) and volume (~1500 m^3) for the inflation source, similar to a previous estimate (100 m and 2500m^3 respectively) (Hamling, 2017).

The persistence of PS through the eruption event shows the dome was not totally destroyed by the eruption, which would have resulted in severe or total temporal decorrelation. However, all time series show a slope decline and large increase in standard deviation immediately following the eruption (Fig. 2). The decline is caused by the rapid, coordinated motion of PS in the dome area, with average motion downward (Fig. 3B) and eastward (Fig. 3D). The increase in standard deviation is consistent with scattering of PS elevations as the previously curved dome (Fig. 4) is deformed to a more uneven surface.

4. Pre-eruption signal (November – December 2019)

To search for a possible pre-eruption signal on the dome, StaMPS processing was repeated for shorter stacks (Table 1) to reduce temporal decorrelation (i.e. improve PS density), while using the north flank datum to provide improved sensitivity to motion on the crater floor. Average displacements for dome PS are plotted as time series (Fig. 5). As with long stacks, time series slopes are positive prior to the eruption, then show large increases in standard deviation immediately afterwards.

Pre-eruption standard deviations for descending short series (average 2.4 mm, see error bars in Fig. 5A & B) are less than corresponding long series (average 3.9 mm, Fig. 2A & B), because standard deviation is a function of PS density. PS density is greater for short series (compare Figs. 2 and 5, n-values in captions give dome area PS counts), because shorter stacks are less subject to temporal decorrelation. The principal of spatial autocorrelation (Moran, 1950) requires the velocities of

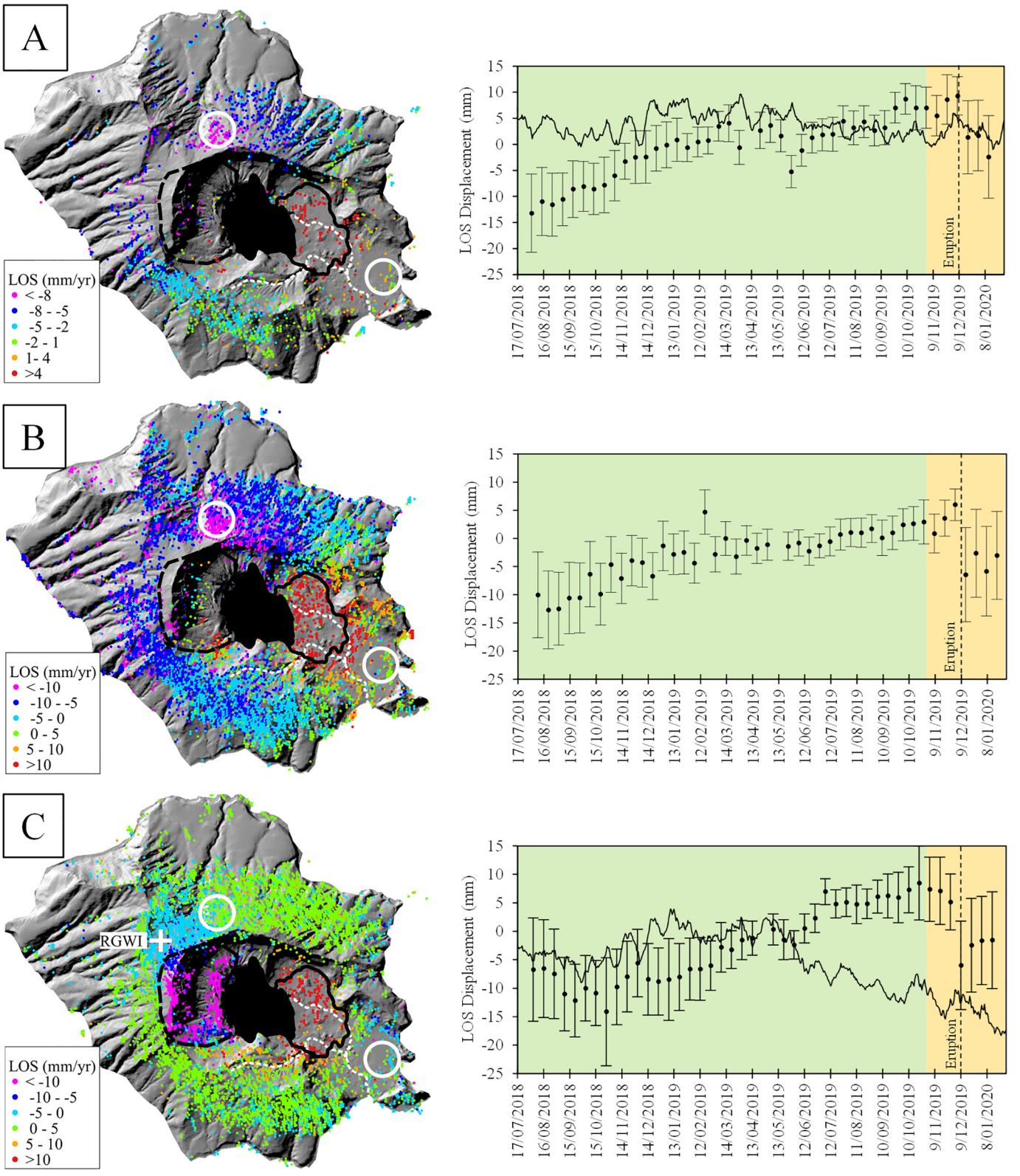

Fig. 2. PS velocity maps for the pre-eruption period (green area in time series), and time series for PS selected from the east-lake zone (solid black boundary). A) descending track #73 (n= 78), B) descending track #175 (n=288), C) ascending track #8 (n=190). Note: time series error bars show ± standard deviation. Dash black line shows west-lake subsidence zone. White circles (100 m radius) show datum areas: RGWC (southeast crater floor) and north flank. White dash line shows tourist trail. Solid black area at centre is the crater lake. Solid black trend line in time series shows vertical motion for RGWC (A) and RGWI (C) continuous monitoring stations (12 day moving average).(For interpretation of the references to color in this figure legend, the reader is referred to the web version of this article.)

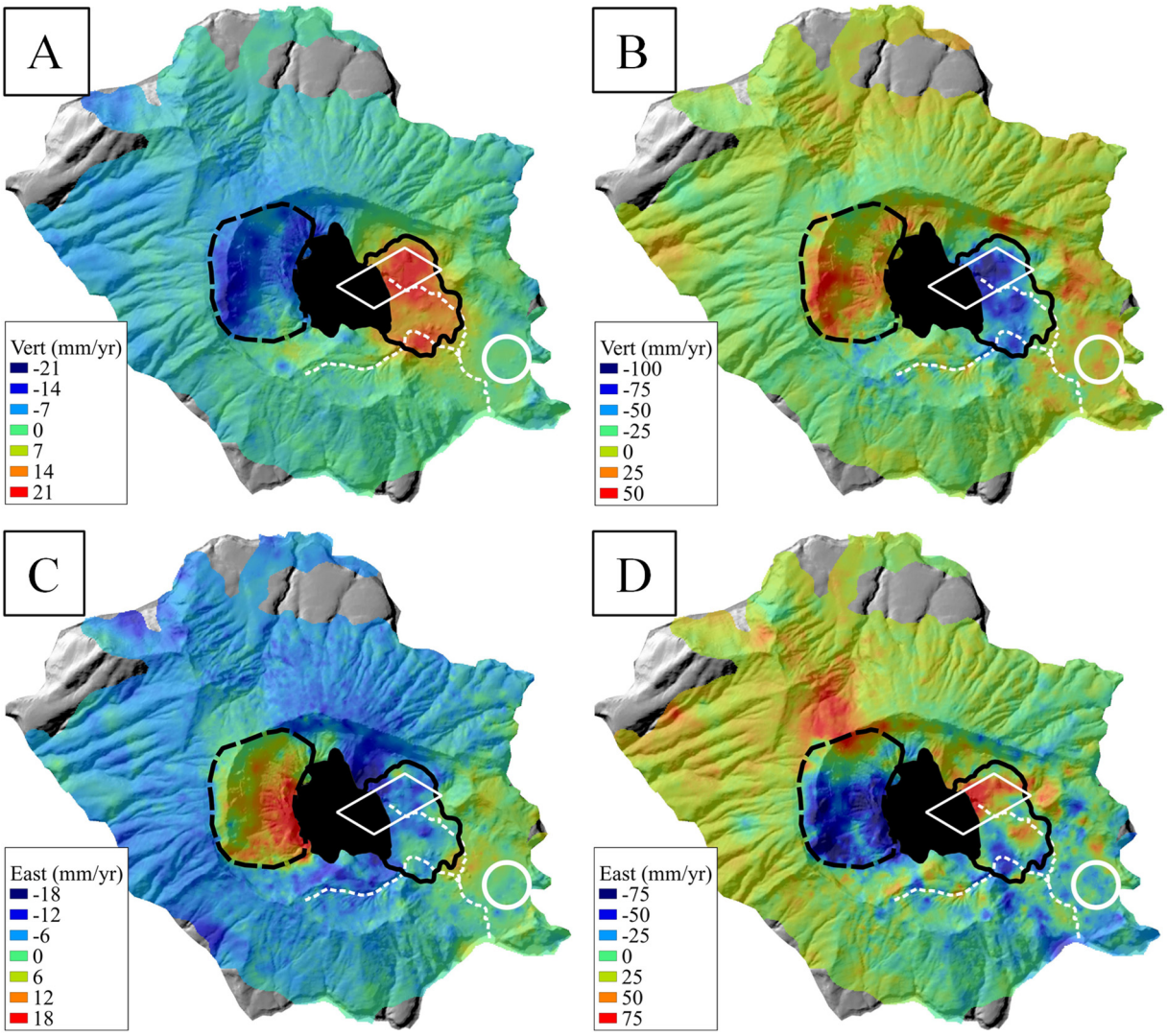

Fig. 3. Deformation maps estimated by combining descending track #175 and ascending track #8. A) vertical motion in the pre-eruption period (green area in Fig. 2 time series), B) vertical motion in the eruption period (orange area in Fig. 2 time series), C) eastward motion in the pre-eruption period, D) eastward motion in the eruption period. Solid black boundary shows east-lake PS selection area for time series (Figs. 2 and 5). Dash black line shows west-lake zone of opposing motion. White circle shows RGWC datum. White dash line shows tourist trail. White parallelogram shows inflation source (Hamling, 2017). Solid black area at centre is the crater lake.(For interpretation of the references to color in this figure legend, the reader is referred to the web version of this article.)

closely spaced PS to be more similar than for distant PS (see variograms in Appendix A, Fig. S2), which explains why shorter series have lower standard deviation. This concept is important because only short time series show a significant drop (i.e. > 1 standard deviation from previous point) prior to the eruption (Fig. 5A and B), signalling dome collapse. The drop is also evident when no datum is specified during StaMPS execution (i.e. StaMPS default execution where the datum is the average motion of the entire island), although the drop is less significant (< 1 standard deviation from previous point) (Appendix A, S6). The time series for ascending track #8 is unstable and does not show a pre-eruption drop (Fig. 5C). Disagreement between ascending and descending LOS time series slopes was previously noted in the dome area following the April 2016 White Island eruption and attributed to strong east-west motion (see P5 and time series in Fig. 2 of Hamling, 2017).

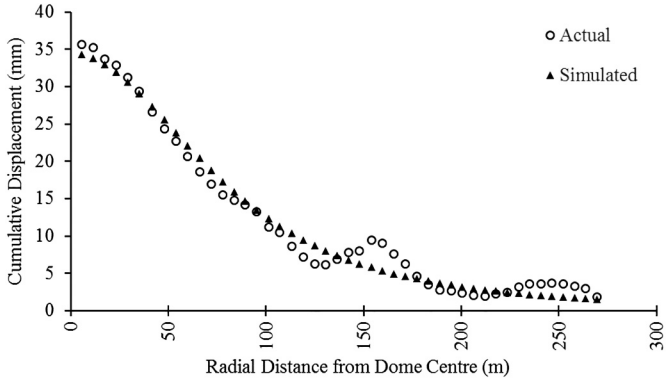

Fig. 4. Best fit Mogi model for crater floor dome from Monte Carlo simulation (1000 realisations).

5. Summary

Sentinel-1 observations over the pre-eruption period showed an inflating dome located on the crater floor to the east of the crater lake. The dome location, and modelled volume/depth for the inflation source are in reasonable agreement with earlier observations, which attributed the inflation to pressurisation of the shallow hydrothermal system.

The eruption period is characterised by a reversal of long-term motions east and west of the crater lake. The dome starts to collapse after

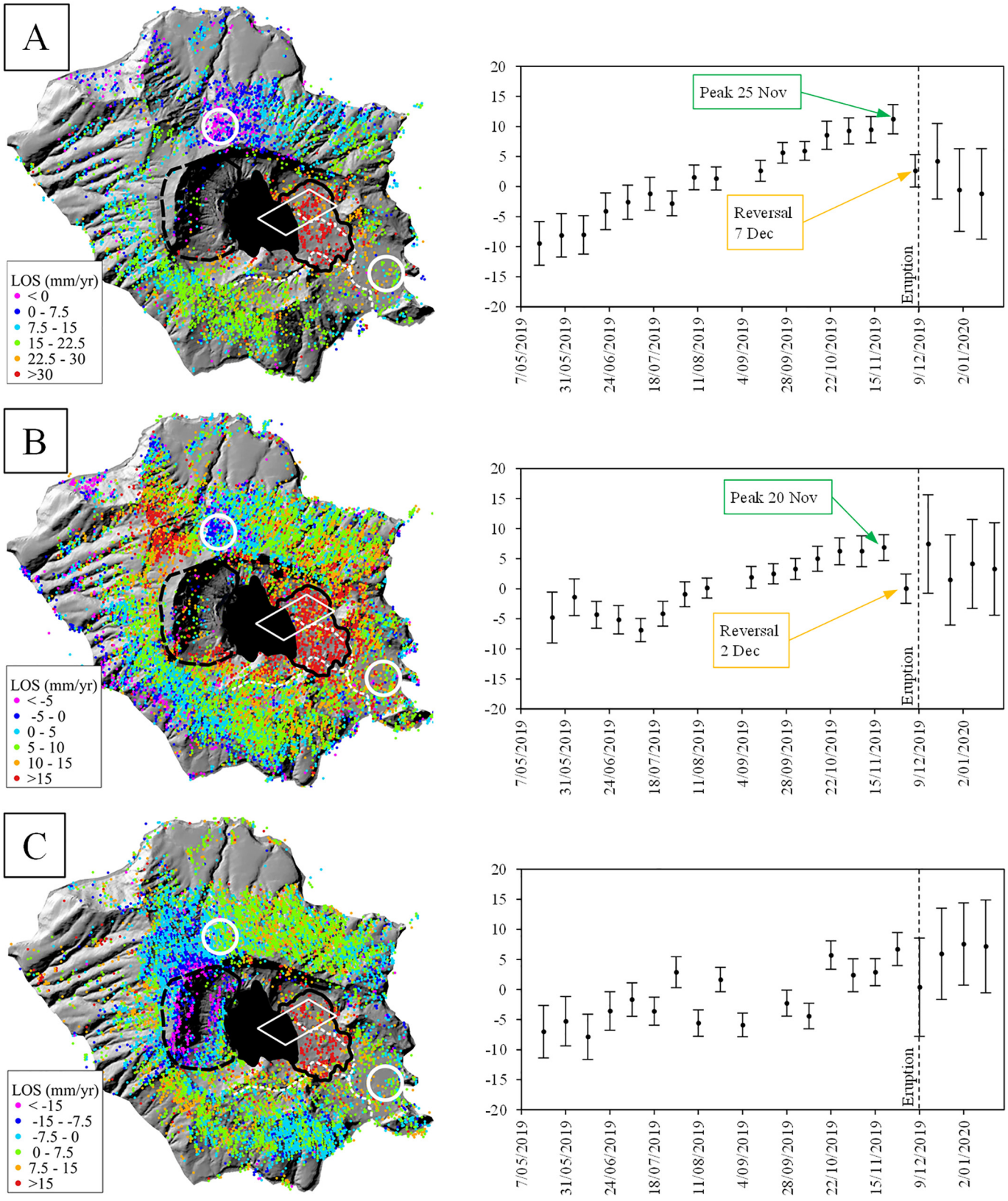

Fig. 5. PS velocity maps for the pre-eruption period, and time series for PS selected from the crater floor dome (solid black boundary). A) descending track #73 (n=281), B) descending track #175 (n=669), and C) ascending track #8 (n=295). Time series error bars show ± standard deviation. Dash black line shows west-lake zone of opposing motion. White circles show datum areas: RGWC (southeast crater floor) and north flank. White dash line shows tourist trail. White parallelogram shows inflation source (Hamling, 2017). Solid black area at centre is the crater lake.

25 November, about two weeks prior to the eruption, probably from depressurisation of the hydrothermal system, while the west-lake area abruptly rises after subsiding during the pre-eruption period.

Horizontal motions also reverse during the eruption period; the dome suddenly moves east, while the west-lake zone moves west. These observations are consistent with intrusion of magma beneath the crater lake area, displacing surrounding volumes and surfaces upward and outward, away from the central conduit. Such a process could also explain the inner-crater uplift zone and west-lake uplift.

GNSS station RGWC shows an unstable time series that might have disguised any deformation signal from the nearby dome collapse, and more subtle inner-crater uplift. In contrast, StaMPS allowed averaging of hundreds of PS time series in the dome area, which revealed inflation then deflation of a dome. Future monitoring of the crater floor should utilise i) short time series in order to reduce temporal decorrelation, ii) both ascending and descending datasets to capture vertical and horizontal motion signals, and iii) a datum outside of the crater in order to provide improved sensitivity to motion on the crater floor.

Declaration of Competing Interest

The authors declare that they have no known competing financial interests or personal relationships that could have appeared to influence the work reported in this paper.

Acknowledgements

Financial support for this research was provided by Waikato Regional Council. The author would like to acknowledge ongoing support by Dr Jim McLeod and Katherine Luketina, and proof reading by Dr Patrick Browne and Dr Colin Harvey.

Appendix A. Supplementary data

Supplementary data to this article can be found online at https://doi.org/10.1016/j.jvolgeores.2020.107124.

References

Cao, Y., Trippanera, D., Li, X., Nobile, A., Yunjun, Z., Passarelli, L., ... Jónsson, S., 2020. InSAR imaging of White Island from 2014 to 2020: Insights into the 2019 Phreatic Eruption. EGU General Assembly Conference Abstracts, p. 10551.

Clark, R., 1973. Surveillance of White Island Volcano, 1968-1972: part 1 volcanic events and deformation of the crater floor. N. Z. J. Geol. Geophys. 16 (4), 949–957.

Clark, R.H., Otway, P.M., 1989. Deformation monitoring associated with the 1976–82 White Island eruption sequence. N. Z. Geol. Surv. Bull. 103, 69–84.

Fournier, N., Chardot, L., 2012. Understanding volcano hydrothermal unrest from geodetic observations: insights from numerical modeling and application to White Island volcano, New Zealand. J. Geophys. Res. Solid Earth 117 (B11).

Geonet, 2019. Volcanic Alert Bulletin WI – 2019/09. https://www.geonet.org.nz/vabs/1prVlz8jGXwWayA8D6Uu5y.

Geonet, 2020a. RGWC (White Island Crater Floor) - Displacement from Initial Position. https://fits.geonet.org.nz/plot?siteID=RGWC&typeID=u.

Geonet, 2020b. RGWC (White Island Crater Floor) - Displacement from Initial Position. https://fits.geonet.org.nz/plot?siteID=RGWI&typeID=u.

Geonet, 2020c. Volcanic Alert Bulletin WI – 2020/3. https://www.geonet.org.nz/vabs/4gbGrPpouFsu3SyO45QLrs.

Giggenbach, W.F., 1987. Redox processes governing the chemistry of fumarolic gas discharges from White Island, New Zealand. Appl. Geochem. 2 (2), 143–161.

Hamling, I.J., 2017. Crater lake controls on volcano stability: insights from White Island, New Zealand. Geophys. Res. Lett. 44 (22), 11311–11319.

Hamling, I.J., 2020. InSAR observations over the Taupō Volcanic Zone's cone volcanoes: insights and challenges from the New Zealand volcano supersite. N. Z. J. Geol. Geophys. 1–11.

Hamling, I.J., Williams, C.A., Hreinsdóttir, S., 2016. Depressurization of a hydrothermal system following the August and November 2012 Te Maari eruptions of Tongariro, New Zealand. Geophys. Res. Lett. 43 (1), 168–175.

Harvey, M.C., Rowland, J.V., Chiodini, G., Rissmann, C.F., Bloomberg, S., Hernández, P.A., Mazot, A., Viveiros, F., Werner, C., 2015. Heat flux from magmatic hydrothermal systems related to availability of fluid recharge. J. Volcanol. Geotherm. Res. 302, 225–236.

Harvey, M., McLeod, J., Luketina, K., Harvey, C., 2019. Geothermal subsidence in Taupo: a comparison of detection methods. Proceedings 41st New Zealand Geothermal Workshop, 25-27 November.

Hooper, A., Zebker, H., Segall, P., Kampes, B., 2004. A new method for measuring deformation on volcanoes and other natural terrains using InSAR persistent scatterers. Geophys. Res. Lett. 31 (23).

Hooper, A., Bekaert, D., Spaans, K., Arıkan, M., 2012. Recent advances in SAR interferometry time series analysis for measuring crustal deformation. Tectonophysics 514, 1–13.

Jolly, A.D., Lokmer, I., Thun, J., Salichon, J., Fry, B., Chardot, L., 2017. Insights into fluid transport mechanisms at White Island from analysis of coupled very long-period (VLP), long-period (LP) and high-frequency (HF) earthquakes. J. Volcanol. Geotherm. Res. 343, 75–94.

Kilgour, G., Gates, S., Kennedy, B., Farquhar, A., McSporran, A., Asher, C., 2019. Phreatic eruption dynamics derived from deposit analysis: a case study from a small, phreatic eruption from Whakāri/White Island, New Zealand. Earth. Planets Space 71 (1), 36.

Malinverni, E.S., Sandwell, D.T., Tassetti, A.N., Cappelletti, L., 2014. InSAR decorrelation to assess and prevent volcanic risk. Eur. J. Remote Sens. 47 (1), 537–556.

Manzo, M., Ricciardi, G.P., Casu, F., Ventura, G., Zeni, G., Borgström, S., ... Lanari, R., 2006. Surface deformation analysis in the Ischia Island (Italy) based on spaceborne radar interferometry. J. Volcanol. Geotherm. Res. 151 (4), 399–416.

Mogi, K., 1958. Relations between the eruptions of various volcanoes and the deformations of the ground surfaces around them. Bull. Earthquake Res. Institute 239, 352–367.

Moran, P.A., 1950. Notes on continuous stochastic phenomena. Biometrika 37 (1/2), 17–23.

Nairn, I.J., Houghon, B.F., Cole, J.W., 1996. Volcanic hazards at White Island. Volcanic Hazards Information SeriesMinistry of Civil Defence.

Nishi, Y., Sherburn, S., Scott, B.J., Sugihara, M., 1996. High-frequency earthquakes at White Island volcano, New Zealand: insights into the shallow structure of a volcano-hydrothermal system. J. Volcanol. Geotherm. Res. 72 (3-4), 183–197.

Osmanoğlu, B., Sunar, F., Wdowinski, S., Cabral-Cano, E., 2016. Time series analysis of InSAR data: methods and trends. ISPRS J. Photogrammetry Remote Sens. 115, 90–102.

Park, I., Jolly, A., Lokmer, I., Kennedy, B., 2020. Classification of long-term very long period (VLP) volcanic earthquakes at Whakaari/White Island volcano, New Zealand. Earth Planets Space 72 (1), 1–10.

Parker, A.L., Biggs, J., Walters, R.J., Ebmeier, S.K., Wright, T.J., Teanby, N.A., Lu, Z., 2015. Systematic assessment of atmospheric uncertainties for InSAR data at volcanic arcs using large-scale atmospheric models: application to the Cascade volcanoes, United States. Remote Sens. Environ. 170, 102–114.

Peltier, A., Hurst, T., Scott, B., Cayol, V., 2009. Structures involved in the vertical deformation at Lake Taupo (New Zealand) between 1979 and 2007: new insights from numerical modelling. J. Volcanol. Geotherm. Res. 181 (3-4), 173–184.

Sherburn, S., Scott, B.J., Nishi, Y., Sugihara, M., 1998. Seismicity at White Island volcano, New Zealand: a revised classification and inferences about source mechanism. J. Volcanol. Geotherm. Res. 83 (3-4), 287–312.

Walsh, B., Procter, J., Lokmer, I., Thun, J., Hurst, T., Christenson, B., Jolly, A., 2019. Geophysical examination of the 27 April 2016 Whakaari/White Island, New Zealand, eruption and its implications for vent physiognomies and eruptive dynamics. Earth Planets Space 71 (1), 25.